Hindawi

Research Article

SLC7A11/GPX4 Inactivation-Mediated Ferroptosis Contributes to the Pathogenesis of Triptolide-Induced Cardiotoxicity

Xian Liu,[1] Cheng Chen,[2] Dong Han,[2] Wei Zhou [ID],[1] Yaowen Cui,[3] Xianglin Tang,[1] Chengrong Xiao,[1] Yuguang Wang [ID],[1] and Yue Gao [ID][1]

[1]*Department of Pharmaceutical Sciences, Beijing Institute of Radiation Medicine, 100850 Beijing, China*
[2]*The Second Medical Center & National Clinical Research Center for Geriatric Diseases, Chinese PLA General Hospital, 100853 Beijing, China*
[3]*School of Pharmacy, Guangdong Pharmaceutical University, 5110006 Guangzhou, China*

Correspondence should be addressed to Yue Gao; gaoyue@bmi.ac.cn

Triptolide exhibits promising efficacy in various cancers and immune diseases while its clinical application has been strongly restricted by its severe side effects, especially cardiotoxicity. However, the underlying mechanism of triptolide-induced cardiotoxicity (TIC) remains unclear. The RNA-seq analysis of triptolide-injured AC16 human cardiomyocyte cell line hinted that ferroptosis is involved in TIC. Further experimental validations proved that triptolide triggered ferroptosis, as evidenced by significant accumulation of lipid peroxidation (4-HNE and MDA levels) and ferrous iron, as well as depletion of intracellular GSH. Furthermore, triptolide-induced iron overload involved the upregulation of TF/TRFC/DMT1 signal axis and the degradation of ferritin, which contribute to ROS generation *via* Fenton reaction. In addition, inhibition of the antioxidant Nrf2/HO-1 pathway was observed in TIC, which may also lead to the overproduction of lethal lipid peroxides. Mechanistically, using streptavidin–biotin affinity pull-down assay and computational molecular docking, we unveiled that triptolide directly binds to SLC7A11 to inactivate SLC7A11/GPX4 signal axis. More importantly, employment of a ferroptosis inhibitor Ferrostatin-1 alleviated TIC by partially reversing the inhibitory effects of triptolide on SLC7A11/GPX4 signal. Altogether, our study demonstrated that SLC7A11/GPX4 inactivation-mediated ferroptosis contributed to the pathogenesis of TIC. Combating ferroptosis may be a promising therapeutic avenue to prevent TIC.

1. Introduction

Traditional Chinese herb *Tripterygium wilfordii* Hook F (TWHF, also known as Thunder God Vine) has been used for centuries in Asian to treat various diseases such as rheumatoid arthritis, lupus, nephrotic syndrome, and Behçet's disease [1]. Triptolide, as the major active component of TWHF, has exhibited potent antirheumatic, anti-inflammatory, immunomodulatory, antitumor, and antimicrobial effects and aroused interests from researchers for decades due to its great efficacy and remarkable clinical performance [2–4]. However, the clinical application of triptolide was limited by its extensive side effects on organs such as the liver, kidney, heart, testes and gastrointestinal tract [5, 6]. The clinical case reports indicated that exposure of triptolide caused cardiac dysfunction [7] such as cardiogenic shock, bradyarrhythmia, and acute toxic myocarditis. In previous acute toxicological studies, histological changes of mice heart tissues (myocardial fiber breakage, cell swelling, interstitial congestion, and so on) and the increase of serum cardiac enzyme (LDH, AST, and CK) level indicated that triptolide caused severe myocardial injuries [8–10]. Additionally, *in vitro* experiments demonstrated that triptolide could induce the death of rat cardiomyocytes at nanomolar concentration [11–13]. Although several research groups have reported the cardiotoxicities of triptolide, the underlying mechanisms of triptolide-induced cardiotoxicity (TIC) have not been fully elucidated.

Ferroptosis is a newly identified type of programmed cell death characterized by the iron-dependent accumulation of

lipid peroxides to lethal levels [14]. Emerging evidences revealed that ferroptosis plays a critical role in various cardiovascular diseases [15, 16] and drug-induced cardiotoxicities [17–19]. However, the association between ferroptosis and TIC remains unclear. As indicated by its name, iron overload is increasingly recognized as the central mediator of ferroptosis [20]. Excessive iron is engaged in free radical formation, especially reactive oxygen species (ROS), by Fenton reaction which results in the initiation and propagation of the lethal lipid peroxides [21]. Intracellular iron homeostasis is precisely regulated by complicated iron metabolism pathways [22, 23]. Initially, extracellular ferric iron (Fe^{3+}) was bound to transferrin (TF) and imported by transferrin receptor 1(TFRC1). As the reduction product of Fe^{3+} in the endosome, ferrous iron (Fe^{2+}) is finally released by divalent metal transporter 1 (DMT1, also termed SLC11A2) from endosome to a liable iron pool in the cytoplasm. In normal condition, excessive ferrous iron will be stored in ferritin, an iron storage protein complex including ferritin light chain (FLT) and ferritin heavy chain (FTH). Pathologically, abnormal iron absorption and storage lead to iron overload which promotes the occurrence of lipid peroxidation and the cell vulnerability to ferroptosis.

SLC7A11/GPX4 pathway functions as the canonical defense against ferroptosis by assisting intracellular glutathione (GSH) synthesis and alleviating lipid peroxidation [24]. SLC7A11 (also known as Xct) is a multipass transmembrane protein which mediates the export of intracellular glutamate and import of extracellular cystine at a 1 : 1 ratio [25]. After absorption inside the cell, cystine is reduced to cysteine which serves as the rate-limiting precursor for glutathione (GSH) synthesis [26]. In the presence of GSH, glutathione peroxidase 4 (GPX4) mediates the conversion of toxic lipid peroxides to nontoxic lipid alcohols [27]. SLC7A11 inhibition results in GSH depletion which in turn downregulates GPX4, leading to cellular/subcellular membrane damage caused by accumulation of iron-dependent lipid peroxides [28]. As the pivotal inhibitory pathway of ferroptosis, SLC7A11/GPX4 axis has attracted enormous attention and been targeted as potential treatment of ferroptosis-related diseases.

In the present study, both bioinformatic analysis and experimental validations proved that ferroptosis played an important role in TIC. Furthermore, we explored the involved molecular mechanism and found that the ferroptosis inhibitor ferrostatin-1 (Fer-1) effectively alleviated TIC. These findings provide new insights into the cell death pathways underlying TIC and suggest a novel therapeutic approach for TIC.

2. Materials and Methods

2.1. Chemicals and Antibodies. Triptolide was purchased from Solarbio Life Science (ST8290, Beijing, China). Triptolide-Biotin were synthesized as described in Supplementary Information. Compounds were dissolved in DMSO at a concentration of 100 mM and stored at -20°C. Ferrostatin-1 (Fer-1) was purchased from Sigma-Aldrich (SML0583, United States). Anti-SLC7A11 rabbit polyclonal antibody (386116) and anti-GLS2 rabbit polyclonal antibody

(163996) were purchased from Zen Bio (Chengdu, Sichuan, China). Anti-GPX4 mouse monoclonal antibody (67763-1-Ig) was purchased from Proteintech (Wuhan, Hubei, China). Anti-4-HNE rabbit polyclonal antibody (ab46545) and anti-β-actin rabbit polyclonal antibody (ab8227) were purchased from Abcam (Cambridge, UK). Anti-Nrf2 rabbit monoclonal antibody (12721S), anti-HO-1 rabbit monoclonal antibody (5853S), anti-GAPDH rabbit monoclonal antibody (5174S), secondary antibody anti-rabbit IgG (7074S), and anti-mouse IgG (7076S) were purchased from cell signaling technology (Danvers, MA, USA).

2.2. Cell Culture. AC16 cells were cultured in Dulbecco's Modified Eagle Medium (DMEM/F12, Gibco) containing 10% fetal bovine serum (FBS, biological industrials (BI)) and 1% penicillin/streptomycin (BI). Cells were maintained in a humidified incubator under 5% CO_2 at 37°C.

2.3. Drug Treatment and Cell Viability Assay. Cell viability was detected using Cell Counting Kit-8 assay (CCK-8, Dojindo, Japan) according to the manufacturer's instruction. AC16 cells were seeded in 96-well plates at a density of 5 $\times 10^3$ cells per well and incubated for 24 h. At 24 h after seeding, cells were, respectively, treated with 0.1% DMSO (control) and triptolide (20-640 nM) or pretreated with Fer-1 (2 μM) for 2 h before exposed to triptolide (30 nM). The final concentration of DMSO never exceeded 1‰ of the total culture volume. After treatment for 24 h, cells were washed with PBS buffer gently and incubated with DMEM/F12 medium containing 10% CCK-8 solution for 1-3 h. Optical density (OD) value was measured with a microplate reader (Multiskan MK3, Thermo Fisher Scientific, United States) at 450 nm.

Cell survival rate = [(OD value of the experimental group − OD value of the blank group)/(OD value of the control group − OD value of the blank group)] × 100%.

2.4. RNA Sequencing and Data Analysis. AC16 cells are treated, respectively, with DMSO (control) and triptolide (30 nM) for 24 h and sent to Novogene Corporation (Beijing, China) for library construction and sequencing. The clustering of the index-coded samples was performed on a cBot Cluster Generation System using TruSeq PE Cluster Kit v3-cBot-HS (Illumia) according to the manufacturer's instructions. After cluster generation, the library preparations were sequenced on an Illumina Nova-seq platform, and 150 bp paired-end reads were generated. In the step of quality data control, clean data were obtained by removing reads containing adapter, reads containing N base, and low quality reads from raw data. All the downstream analyses were based on the clean data with high quality. Differential expression analysis of two conditions/groups (two biological replicates per condition) was performed using the DESeq2 R package (1.20.0). DESeq2 provide statistical routines for determining differential expression in digital gene expression data using a model based on the negative binomial distribution. The resulting p values were adjusted using the Benjamini and Hochberg's approach for controlling the false discovery rate. Genes with an adjusted p value < 0.05

found by DESeq2 were assigned as differentially expressed. KEGG (Kyoto Encyclopedia of Genes and Genomes) is a database resource for understanding high-level functions and utilities of the biological system, such as the cell, the organism, and the ecosystem, from molecular-level information, especially large-scale molecular datasets generated by genome sequencing and other high-through put experimental technologies (https://www.genome.jp/kegg/). We used clusterProfiler R package to test the statistical enrichment of differential expression genes in KEGG pathways.

2.5. Determination of Intracellular Iron Levels. The intracellular iron concentration was detected by the iron ion colorimetric detection kit (E1042, Applygen Technologies, Beijing, China). The AC16 cells were seeded in 24-well plates at a density of 5×10^4 cells per well. At seeding after 24 h, cells were exposed to DMSO (control) and triptolide (30 nM) or pretreated with DFO (50 μM) for 2 h before cotreated with triptolide (30 nM). After treatment for 24 h, cells were washed with cold PBS buffer twice and lysed with RIPA buffer for 2 h. According to the manufacturer's instruction, a standard stock solution was prepared immediately using the dilute solution. Mixture A was prepared by mixing the buffer solution with 4.5% potassium permanganate solution at the ratio of 1 : 1. Next, thoroughly mix the sample with the detection working solution, and incubate at 60°C for 1 h. At the end of the incubation, the iron ion detection reagent was added and incubated at room temperature for 30 minutes. 200 μL of the final solution was added to a 96-well plate per well, and the concentration of iron ions in the cells was detected at 550 nm using a microplate reader (Multiskan MK3, Thermo Fisher Scientific, USA). The intracellular iron levels were then normalized by cell numbers.

2.6. Measurement of Malonaldehyde (MDA) and Glutathione Levels. Lipid peroxidation MDA assay kit (S1031S) were purchased from Beyotime (Jiangsu, China). In brief, cells were sonicated in RIPA buffer on ice. Cell lysates were then centrifuged at 12,000 g for 15 min at 4°C to collect the supernatant. MDA levels were measured using a lipid peroxidation MDA assay kit according to the manufacturer's instruction and detected at 532 nm using a microplate reader (Multiskan MK3, Thermo Fisher Scientific, USA). MDA levels were normalized by the protein concentration. GSH levels were measured by a microreduced glutathione (GSH) assay kit (Solarbio Life Science, BC1175, Beijing, China) according to the manufacturer's instruction and detected 412 nm using a microplate reader (Multiskan MK3, Thermo Fisher Scientific, USA). The GSH levels were further normalized by cell numbers.

2.7. Measurement of Intracellular ROS Levels. ROS levels was measured by flow cytometry using DCFH-DA probe (S0033S, Beyotime, Jiangsu, China). Cells were treated, respectively, with DMSO (control) and triptolide (7.5, 15, 30, and 60 nM). After treatment for 24 h, cells were collected and incubated in DMEM/F12 medium containing DCFH-DA (10 μM, 20 mins) at 37°C in the dark. Cells were washed with DMEM/F12 medium three times. The samples were then analyzed with a FACStar-Plus flow cytometer (Becton Dickinson, Franklin Lakes, NJ, USA) and the FlowJo (TreeStar) software for acquisition and analysis.

2.8. Protein Extraction and Western Blot. After treatment, cells were harvested and lysed with RIPA buffer (C1053, Applygen Technologies, Beijing, China) containing protease/phosphatase inhibitor cocktail (GRF101/102, EpiZyme, Shanghai, China). Protein concentrations were determined using a BCA assay kit (P1511, Applygen Technologies, Beijing, China). Protein samples were separated by SDS-PAGE gels and transferred onto polyvinylidene fluoride membranes (Millipore, Billerica, MA, United States). After blocked with 5% nonfat milk for 1 h, the membranes were incubated successively with specific primary and secondary antibodies. The protein blots were visualized with "Torchlight" Hypersensitive ECL Western HRP Substrate (17046, Zen Bio, Chengdu, China) and automatic exposure system (Image Quant LAS500, GE, Fairfield, CT, USA).

2.9. Streptavidin–Biotin Affinity Pull-Down Assay. The biotin-affinity pull-down assay was performed as previously described [29, 30]. Triptolide-biotin were synthesized and verified by ^{1}H and ^{13}C NMR (see Supplementary Information (available here)). AC16 cells were lysed with RIPA buffer (C1053, Applygen Technologies, Beijing, China) containing protease/phosphatase inhibitor cocktail (GRF101/102, EpiZyme, Shanghai, China) and centrifuged at 12,000 g for 15 min at 4°C to collect the supernatant. The cell lysates were incubated, respectively, with biotin (10 μM), triptolide-biotin (10 μM), and the combination of triptolide (100 μM) and triptolide-biotin (10 μM) for 12 h at 4°C. The magnetic beads (MCE) were then added to the cell lysates and incubated for 4 h at 4°C. The supernatant was removed, and the magnetic beads were boiled in SDS-PAGE sample buffer. The samples were tested by immunoblot with indicated antibodies.

2.10. Molecular Docking. The 3D structures of triptolide were drawn by ChemBioDraw Ultra 20.0 and then subjected to energy optimization by the MM2 force field. The 3D structure of 7CCS was downloaded from the PDB (https://www.rcsb.org/pdb/home/home.do) [31, 32]. The ligand and protein files were prepared using AutoDock tools. The protein was optimized by removing water molecules, adding hydrogen, and adding Geister charges, and protein file was saved in PDBQT format. Ligand file was also saved in PDBQT format. The protein-ligand grid map was calculated surrounding active site of protein molecule. Molecular docking analysis were carried out by Autodock Vina. Autodock Vina was run using configuration file and output file generated contained theoretical binding affinity. The lesser binding affinity corresponds to better results. The docking results were visualized using PyMol.

2.11. Statistical Analysis. All results were presented as mean ± standard deviation (SD) and generated from at least three independent experiments. Comparison between two or more groups was performed using the Student's t test
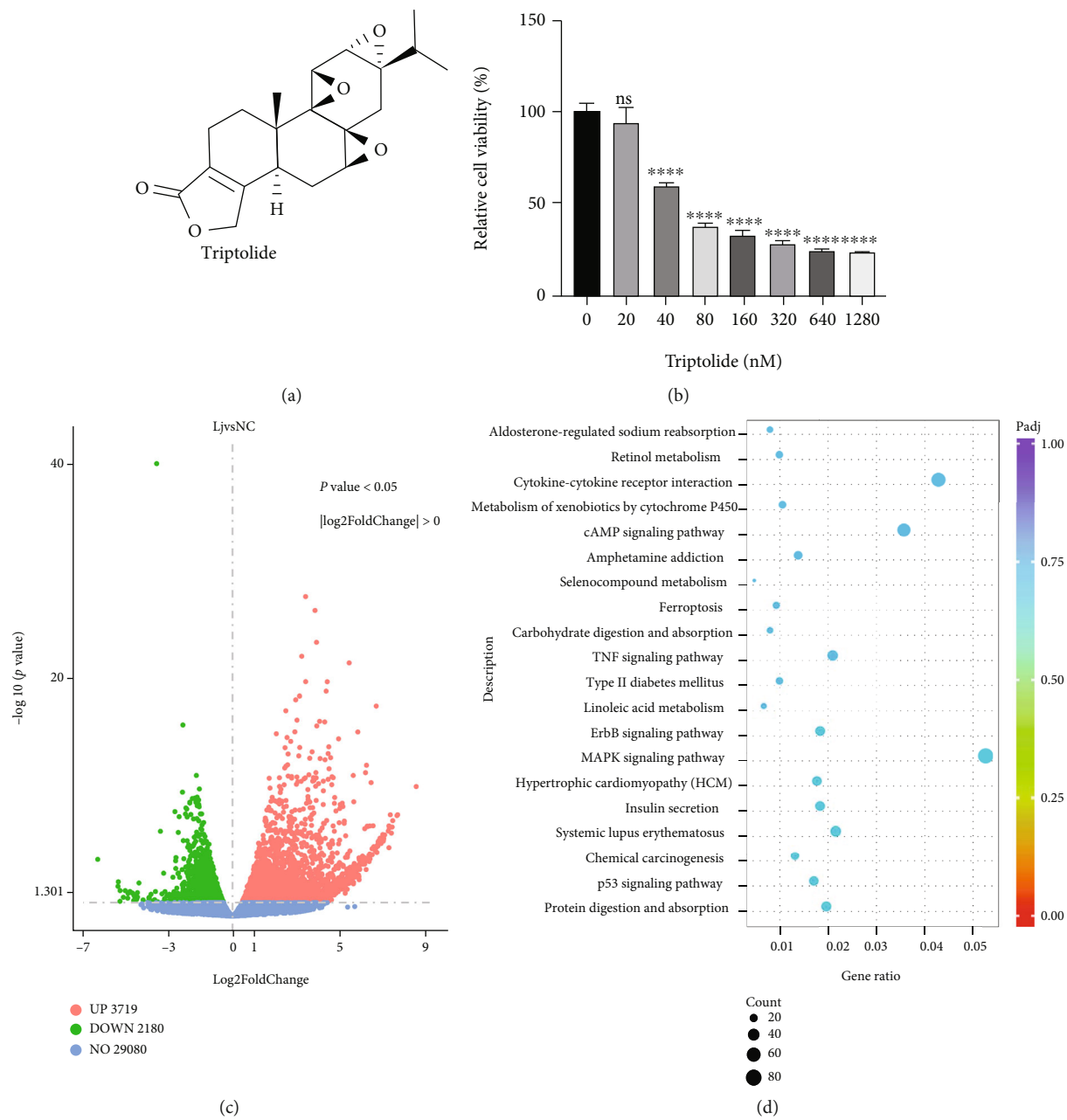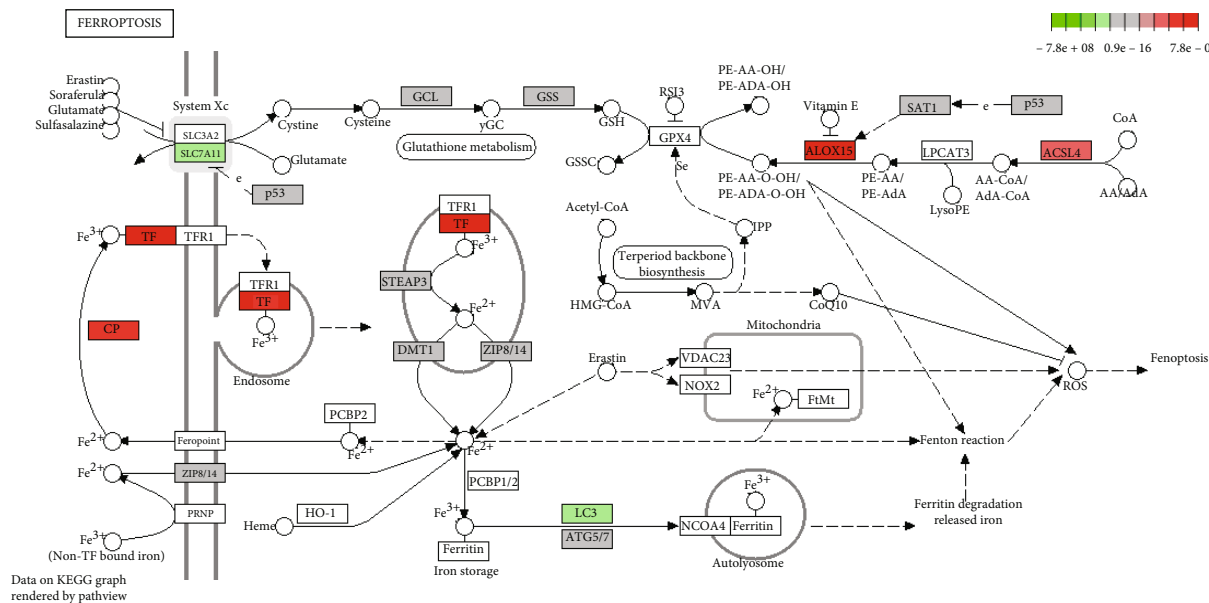
(a)

(b)

(c)

(d)

FIGURE 1: Continued.

FERROPTOSIS

Erastin
Soraferula
Glutamate
Sulfasalazine

System Xc

SLC3A2
SLC7A11

Cystine — Cysteine — yGC — GSH

GCL   GSS

Glutathione metabolism

Glutamate

p53

GSSG — GPX4

RSI3

PE-AA-OH/
PE-ADA-OH

Se

PE-AA-O-OH/
PE-ADA-O-OH

Vitamin E

ALOX15

SAT1   e   p53

LPCAT3   ACSL4   CoA

PE-AA/
PE-AdA

AA-CoA/
AdA-CoA   AA/AdA

LysoPE

Acetyl-CoA

IPP

Terperiod backbone
biosynthesis

HMG-CoA — MVA — CoQ10

Fe^{3+} TF   TFR1

TFR1
TF Fe^{3+}

STEAP3

Fe^{2+}

DMT1   ZIP8/14

TFR1
TF

Fe^{3+}

CP

Endosome

Mitochondria

Erastin

VDAC23

NOX2 Fe^{2+} FtMt

ROS — Fenoptosis

Fe^{2+} Feropoint

PCBP2 Fe^{2+}

Fe^{2+}

PCBP1/2

Fenton reaction

Ferritin degradation
released iron

Fe^{2+} ZIP8/14

PRNP   Heme   HO-1 Fe^{3+}

Fe^{3+}
(Non-TF bound iron)

Ferritin

Iron storage

LC3
ATG5/7

NCOA4   Ferritin

Fe^{3+}

Autolyosome

Data on KEGG graph
rendered by pathview

−7.8e + 08   0.9e − 16   7.8e − 0

(e)

Gene Symbol	Gene ID	log2FoldChange (LJvsNC)	protein encoded
ALOX15	ENSG00000161905	7.316086279	Arachidonate 15-lipoxygenase
TF	ENSG00000091513	6.447771903	Transferrin
SLC38A1	ENSG00000111371	4.162763405	Solute carrier family 38 member 1
GLS2	ENSG00000135423	3.848331429	Glutaminase 2
ALOX5	ENSG00000012779	3.785913825	Arachidonate 5-lipoxygenase
ALOX12B	ENSG00000179477	2.908585929	Arachidonate 12-lipoxygenase, 12R type
DPP4	ENSG00000197635	2.547712017	Dipeptidyl peptidase 4
DUOX2	ENSG00000140279	2.241442559	Dual oxidase 2
ATF3	ENSG00000162772	2.170294655	Activating transcription factor 3
MAP1LC3A	ENSG00000101460	2.131140382	Microtubule associated protein 1 light chain 3 alpha
CDO1	ENSG00000129596	1.799825998	Cysteine dioxygenase type 1
MYB	ENSG00000118513	1.749191747	MYB proto-oncogene
TFR2	ENSG00000106327	1.446275597	Transferrin receptor 2
NOX5	ENSG00000255346	1.438180842	Nicotinamide adenine dinucleotide phosphate oxidase 5
CYBB	ENSG00000165168	1.21503239	Cytochrome b-245 beta chain
MIOX	ENSG00000100253	1.049176639	Myo-inositol oxygenase
SOCS1	ENSG00000185338	1.043587247	Suppressor of cytokine signaling 1
DUOX1	ENSG00000137857	1.022957204	Dual oxidase 1
TNFAIP3	ENSG00000118503	0.931576903	TNF alpha induced protein 3
ALOXE3	ENSG00000179148	0.876721036	Arachidonate lipoxygenase 3
ACSF2	ENSG00000167107	0.771924716	Acyl-CoA synthetase family member 2
TLR4	ENSG00000136869	0.711988592	Toll like receptor 4
TP53	ENSG00000141510	0.681397191	Tumor protein p53
MAPK9	ENSG00000050748	0.600246955	Mitogen-activated protein kinase 9
GABARAPL1	ENSG00000139112	0.536478583	GABA type A receptor associated protein like 1
ULK2	ENSG00000083290	0.510948818	Unc-51 like autophagy activating kinase 2
ATG16L1	ENSG00000085978	0.476287427	Autophagy related 16 like 1
SIRT1	ENSG00000096717	0.43785615	Sirtuin 1
ZEB1	ENSG00000148516	0.427187358	Zinc finger E-box binding homeobox 1
SAT1	ENSG00000130066	0.33777489	Spermidine/spermine N1-acetyltransferase 1
WIPI2	ENSG00000157954	0.264630585	WD repeat domain, phosphoinositide interacting 2
ALOX12	ENSG00000108839	0.251306556	Arachidonate 12-lipoxygenase, 12S type
ALOX15B	ENSG00000179593	0.139746069	Arachidonate 15-lipoxygenase type B
ATG13	ENSG00000175224	0.120877503	Autophagy related 13
NCOA4	ENSG00000266412	0.107375892	Nuclear receptor coactivator 4
DNAJB6	ENSG00000105993	0.106623575	DnaJ heat shock protein family (Hsp40) member B6
ACVR1B	ENSG00000135503	0.086813153	Activin A receptor type 1B
ATM	ENSG00000149311	0.073769126	ATM serine/threonine kinase
MAPK1	ENSG00000100030	0.057016614	Mitogen-activated protein kinase 1
PANX1	ENSG00000110218	0.056449946	Pannexin 1
ATG4D	ENSG00000130734	0.051089607	Autophagy related 4D cysteine peptidase
LPCAT3	ENSG00000111684	0.010402338	Lysophosphatidylcholine acyltransferase 3

(f)

FIGURE 1: Continued.

Gene Symbol	Gene M	Iog2FoldtCasge (LjvsNC)	protein encoded
CBS	ENS000000160200	−1.882238865	Cystathimuue beta-synthase
SLC7A11	ENSG0000151012	−1.807653378	Solute carrier family 7 tuember 11
T6IBLM4	ECSG00000155957	−1383391925	Transmembeaue BAX inhibitor motif containing 4
N'F2	ENS0000186575	−1.115279397	Neurofibromin 2
SCD	ENS000000099194	−1.112051021	Stcaroyl-CoA desulfurase
NTS1	ENS000000244005	−1.0894305	NFSI cysteine desulfurase
ATF4	ENS000000128272	−1.080955719	Activating transcription factor 4
JUN	EN5000000177606	−0.858723893	Junproto-oncogene, AP-1 transcription factor subunit
AKRIC2	ENSG00000151.632	−0.805928939	Aldo-keto reductase family 1 member C2
AIF342	ENS000000042256	−0.693286418	Apopcosis inducing factor mitochondria associated 2
CISD1	EN80000000122873	−0.417422626	CDGSH iron sulfur domain 1
SQSTMI	ENS000000161011	−0.412733884	Sequestosome 1
FT111	ECSG00000167996	−0.379757176	Ferritin heavy chair 1
OTUBI	ENSG00000167770	−0.338278195	deubiquitinase. ubiquitio aldehyde binding 1
MTOR	ENSG0000198793	−0.336470136	kiechaaistic target of rapamycin kinase
HSPBI	ENS000000106211	−0.303527509	Heat shock protein /acuity B (Small) member 1
BRD4	ENSG00000141867	−0.276951271	Bromodomaia containing 4
FANCD2	EN5000000144554	−0.261207043	FA complementation group D2
GPX4	ENSG00000167468	−0235060457	Glotathione peroxidase 4
PML	ECSG00000140464	−0.198882461	Promyelocytic leukemia
HSPAS	ENS000000044574	−0.178057704	Heat shock wain family A (Hsp70) member 5
ACSL3	ENS000000123983	−0.159581498	Acyl-CoA synthetase long chain family member 3
CAVI	ENSG00000105974	−0.133672868	Caveolin 1
GCLC	ENS000000001084	−0.126747309	Glutamate-cysteint ligast catalytic subunit
CHMP6	ENS000000176108	−0.124897137	Charged multivesicular body protein 6
HSF1	ENSG000001135122	−0.118848246	Heat shock transcription factor 1
N1E2L2	E1CS000000116044	- −0.103434024	Nuclear factor embroid 2 like

(g)

FIGURE 1: Triptolide induces ferroptosis in AC16 cells indicated by RNA-seq analysis. (a) Chemical structure of triptolide. (b) Cell viability of AC16 cells after treatment with triptolide for 24 h was detected using CCK-8 assay. ns: no significant; $^{****} p < 0.0001$ vs. the control group. (c) Triptolide-induced differentially enriched genes. (d) Top 20 KEGG pathway with high count. (e) Main targets of triptolide in ferroptosis. (f) DEGs identified as ferroptosis diver in FerrDb. (g) DEGs identified as ferroptosis suppressor in FerDb.

and ANOVA for normal variables or the Mann–Whitney U test and Kruskal-Wallis test for nonnormal variables that could not be log transformed (e.g., because of frequent zero values). A value of $p < 0.05$ was chosen as the threshold for statistical significance. Statistical analysis was performed using GraphPad Prism version 8 (GraphPad Software, La Jolla, CA).

3. Results

3.1. Triptolide Potentially Induces Ferroptosis in AC16 Cells. The chemical structure of triptolide is shown in Figure 1(a). To determine the cytotoxicity of triptolide on human cardiomyocytes, AC16 cells were exposed to multiple concentrations of triptolide (0-1280 nM, Figure 1(b)) for 24 h. The CCK-8 results showed that triptolide exhibited significant inhibitory effects on the cell viability of AC16 cells in a dose-dependent manner. To investigate the underlying mechanism of TIC, AC16 cell post triptolide (30 nM) stimulation for 24 h was subjected to the RNA sequencing (RNA-seq) analysis. As shown in the volcano plot (Figure 1(c)), there were a total of

5899 differentially expressed genes (DEGs) (|Fold change| > 2, p value < 0.05, 3719 genes upregulated, and 2180 genes downregulated). KEGG enrichment analysis suggested that ferroptosis emerged as the main cell death form in the process of TIC (Figure 1(d)). KEGG graph of ferroptosis (Figure 1(e)) showed that genes related with GSH, iron, and polyunsaturated fatty acid metabolism, such as SLC7A11, TF, and ACSL4, were involved in the process. Furthermore, we overlapped DEGs with genes identified as ferroptosis driver and suppressor in ferroptosis database FerrDb [33]. DEGs which change trends were in coincidence with ferroptosis driver and suppressor were, respectively, listed in Figures 1(f) and 1(g), including lipid peroxidation related-genes (ALOX15, ALOX5, ALOX12, NOX5, DUOX1, and DUOX2), glutathione metabolism genes (SLC7A11, GLS2, and GPX4), and iron metabolism genes (TF, FTH1, NCOA4, and MAP1LC3A). Overall, these results suggested a role of ferroptosis in the pathogenesis of TIC.

3.2. Triptolide Provokes Lipid Peroxidation, Excess Iron Accumulation, and GSH Depletion. To validate the role of
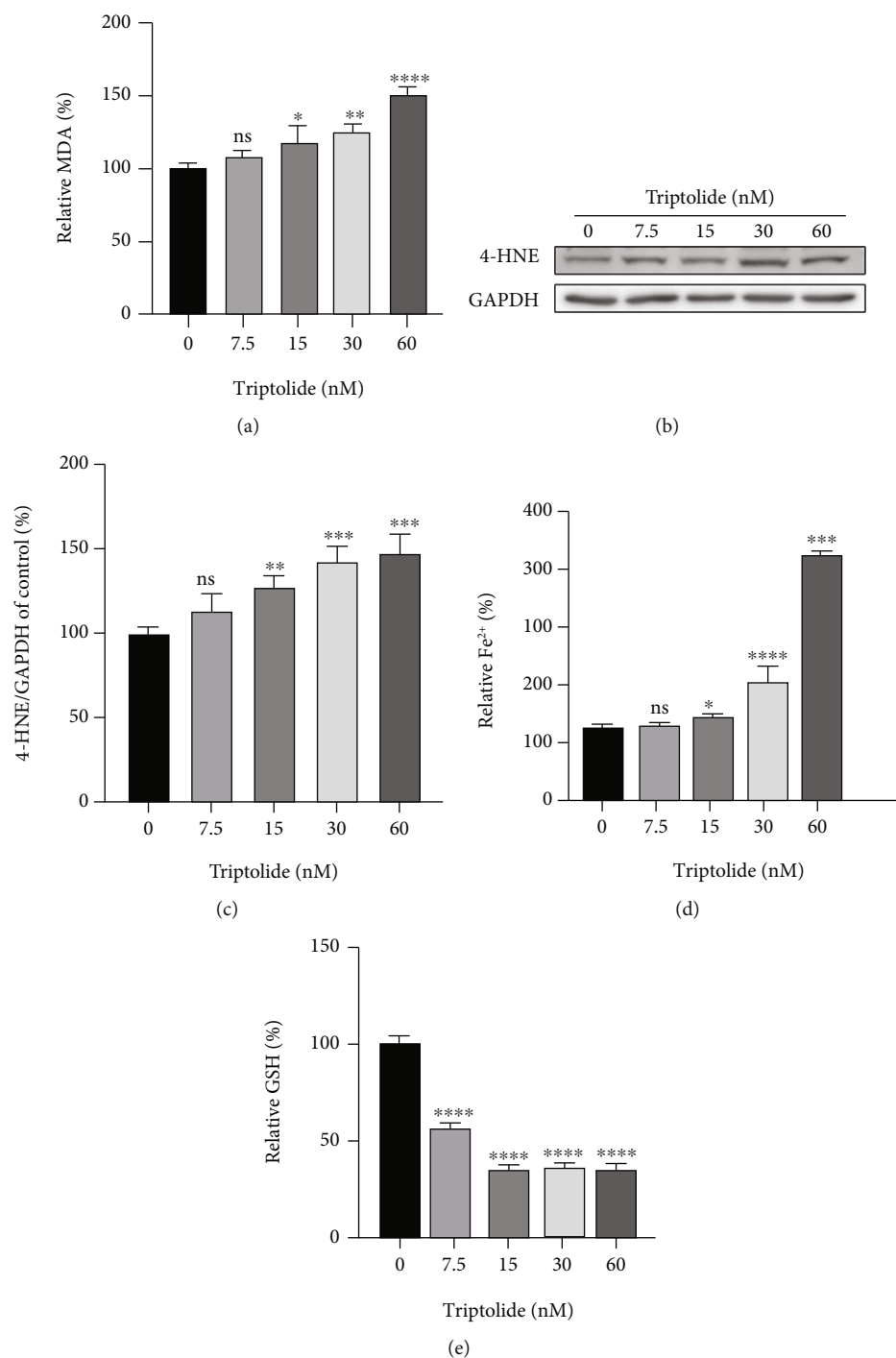
FIGURE 2: Triptolide provokes lipid peroxidation, excess iron accumulation, and GSH depletion. (a) MDA levels after treatment with triptolide for 24 h were detected by commercial assay kits. (b, c) The protein levels of 4-HNE were measured by Western blots. (d) Intracellular Fe^{2+} levels in AC16 cells. (e) Reduced GSH levels in AC16 cells. ns: no significant; $^*p < 0.05$, $^{**}p < 0.01$, $^{***}p < 0.001$, $^{****}p < 0.0001$ vs. the control group.

ferroptosis in TIC, we assessed the key features of ferroptosis including lipid peroxidation, excess iron accumulation, and GSH depletion [34]. As the most prevalent byproduct of lipid peroxidation, MDA levels increased dose-dependently after treatment with triptolide for 24 h (Figure 2(a)). Additionally, Western blot results showed that the expression of 4-HNE, a classic indicator of ferroptosis-induced lipid hydroperoxides, was gradually elevated as the increase of triptolide concentration (Figures 2(b) and 2(c)). Moreover, the accumulation of intracellular ferrous iron was induced significantly upon the stimulation of triptolide (Figure 2(d)). Contrary to iron levels, GSH, as the most abundant intracellular antioxidant, decreased

(a)

(b)

(c)

(d)

(e)

(f)
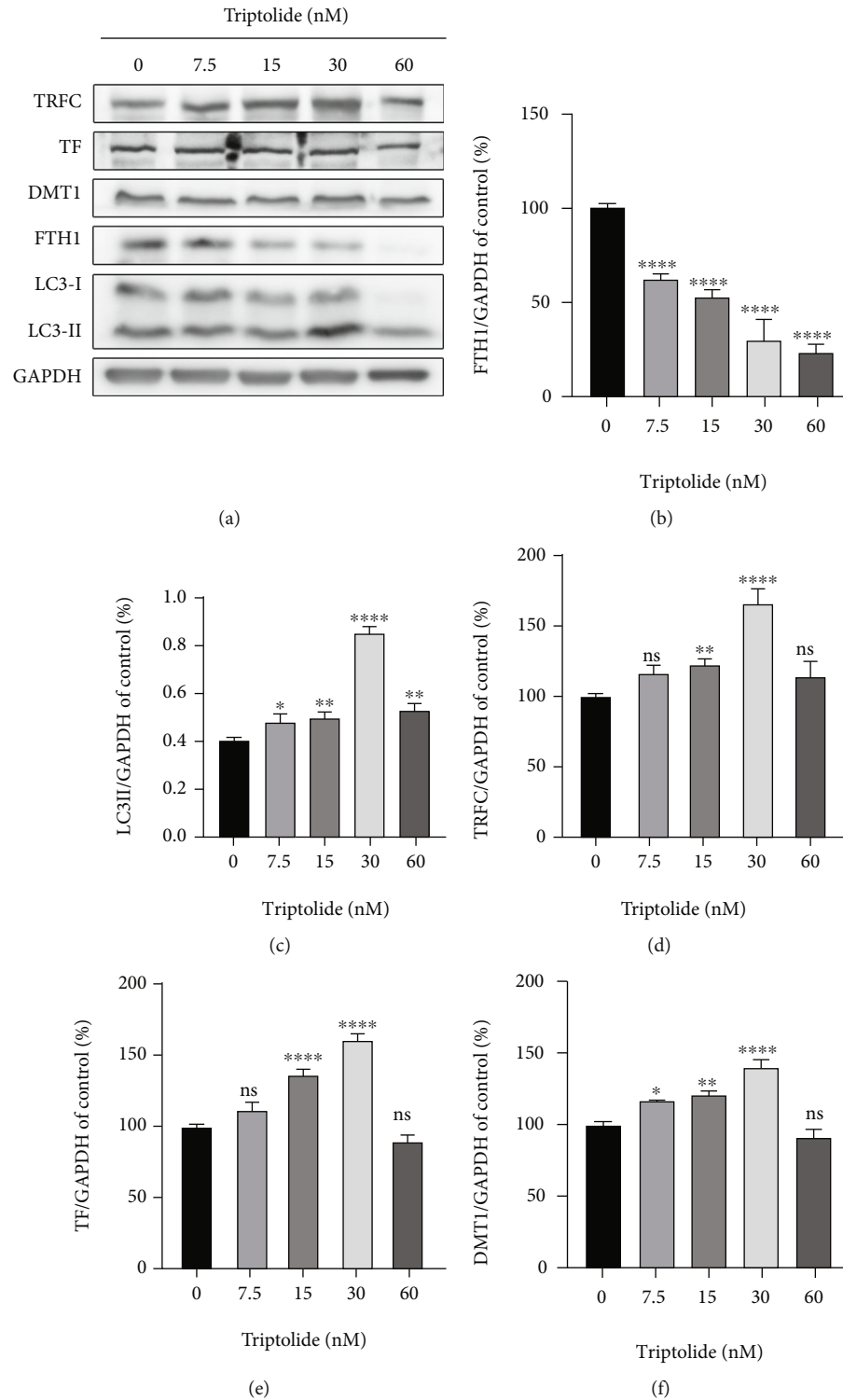
FIGURE 3: Triptolide triggers iron overload through dysregulating iron absorption and storage system. (a) The protein levels of TRFC, TF, DMT1, FTH1, and LC3-II in AC16 cells were measured by Western blots. (b–f) The quantitative analysis of the indicated proteins. ns: no significant; $^*p < 0.05$, $^{**}p < 0.01$, $^{***}p < 0.001$, $^{****}p < 0.0001$ vs. the control group.

dramatically in the presence of triptolide (Figure 2(e)). Collectively, these data validate that ferroptosis is involved in TIC.

3.3. Triptolide Triggers Iron Overload through Dysregulating Iron Absorption and Storage System. As the central mediator

of ferroptosis, cumulative ferrous iron produces excess ROS by Fenton reaction to rapidly amplify lipid peroxides [14, 15]. To unveil the intrinsic molecular mechanism of iron overload, we assessed the expression of genes associated with intracellular iron storage and extracellular iron absorption.
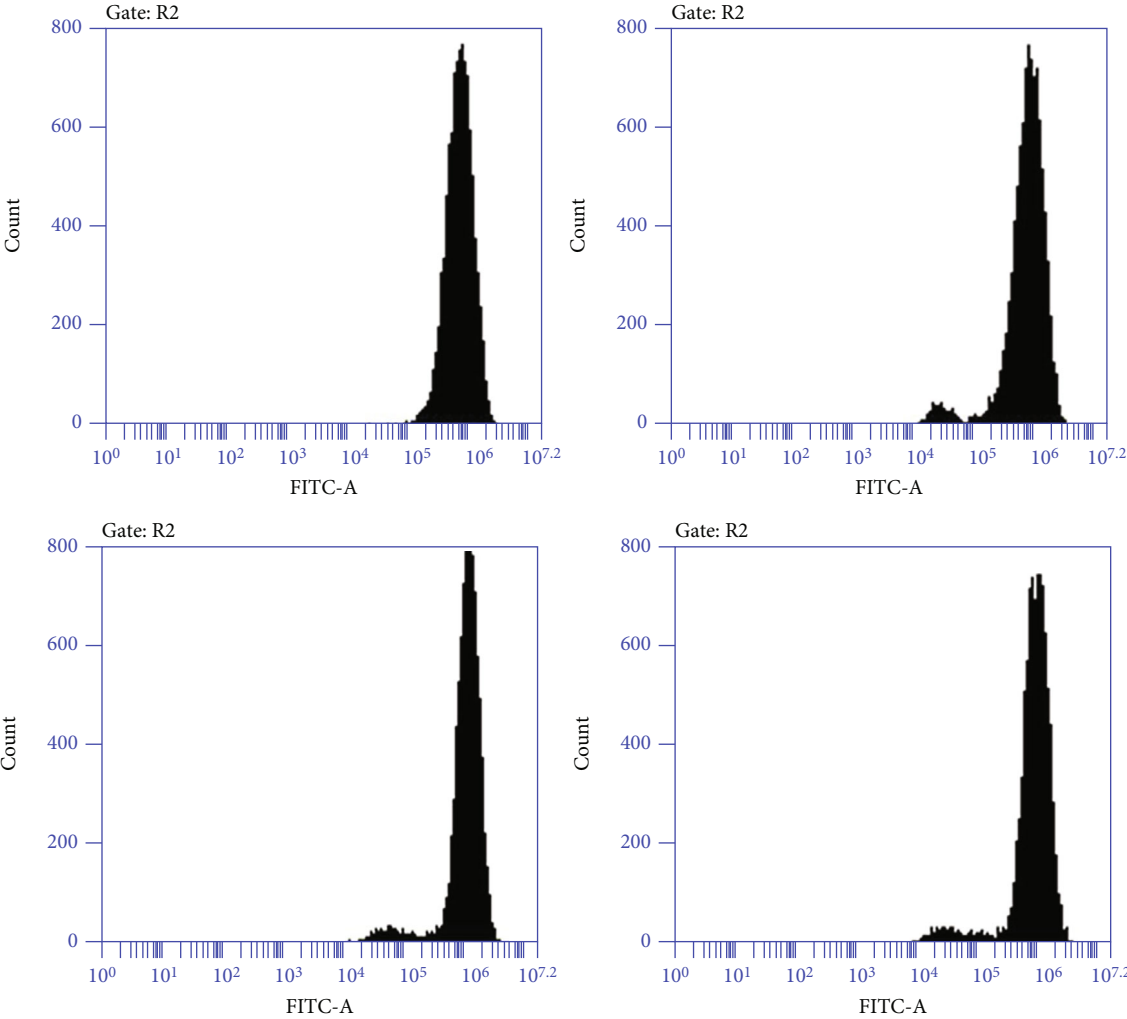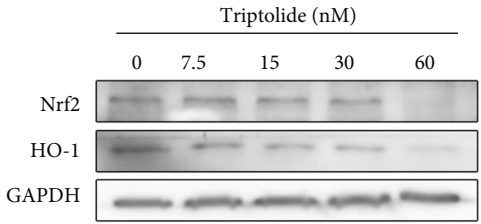
(a)
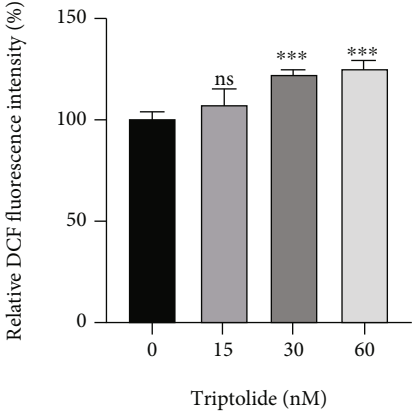
(b)

(c)
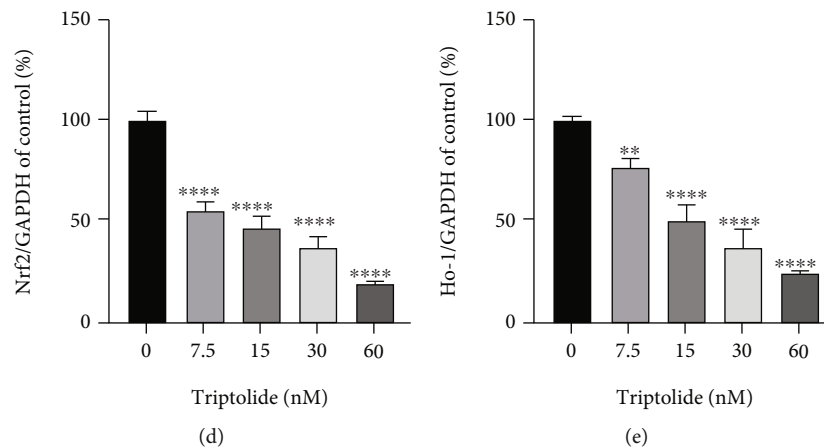
FIGURE 4: Continued.

(d)

(e)

FIGURE 4: Triptolide aggravated ROS accumulation *via* inhibiting Nrf2/HO-1 pathway. (a, b) ROS levels were assessed by flow cytometry using DCFH-DA probe. (c) The protein levels of SLC7A11 and GPX4 were measured by Western blots. (d, e) The quantitative analysis of the indicated proteins. ns: no significant; $^*p < 0.05$, $^{**}p < 0.01$, $^{***}p < 0.001$, $^{****}p < 0.0001$ vs. the control group.

After treatment with triptolide (0-60 nM), the expression of FTH1 decreased dose-dependently, paralleling a significant increase of LC3II/I ratio, indicating ferritin was degraded to release ferrous iron in an autophagic manner [35, 36] (Figures 3(a)–3(c)). Besides, Western blot results showed that the expression of TF, TRFC, and DMT1, the genes in charge of iron import, was upregulated in a dose-dependent way after treatment with triptolide (0-30 nM) (Figures 3(d)–3(f)). However, an unexpected decrease of these iron import proteins was detected when AC16 cells were treated with an even higher concentration of triptolide (60 nM).

3.4. Triptolide Aggravates ROS Accumulation and Inhibited Nrf2/HO-1 Pathway.

As increased level of ROS is often accompanied by iron overload, we examined the intracellular ROS levels of AC16 cells with triptolide (0-60 nM) for 24 h. Flow cytometry using DCFH-DA probe showed that triptolide promoted ROS levels significantly in a dose-dependent way (Figures 4(a) and 4(b)). As Nrf2/HO-1 is considered as the classic antioxidant pathway participating in ferroptosis regulation [37], we next assessed the alteration of Nrf2/HO-1 signal axis. Western blot results showed that the expression of Nrf2 and HO-1 decreased significantly as the raise of triptolide treatment concentration, suggesting the inhibitory effects of triptolide on Nrf2/HO-1 pathway exacerbated ROS accumulation in human cardiomyocytes (Figures 4(c)–4(e)), which succumbed cells to ferroptosis through generation of excess lipid peroxides.

3.5. Triptolide Downregulates SLC7A11/GPX4 Axis by Direct Binding to SLC7A11.

SLC7A11/GPX4 axis is recognized as the primary defense mechanism against ferroptosis due to its potent function to deoxify excess lipid peroxides with the help of GSH. Therefore, we explored the expression of SLC7A11/GPX4 axis after treatment with triptolide for 24 h. As shown in Figures 5(a)–5(c), SLC7A11/GPX4 axis was remarkably inhibited in response to triptolide treatment. Furthermore, to investigate the direct target by which triptolide inhibited SLC7A11/GPX4 axis, we labelled triptolide

with biotin through esterification reaction (Figure 5(d)). Triptolide was incubated with streptavidin beads and AC16 cell lysates. Western blot results indicated that SLC7A11 is a bona fide binding partner of triptolide in triptolide-treated AC16 cells (Figure 5(e)). This result was further validated by molecular docking. As shown in the modeling, molecular docking [38, 39] also demonstrated triptolide interacted with the amino acid residues on SLC7A11 by van der Waals, carbon hydrogen bond, and conventional hydrogen bond (Figures 5(f) and 5(g)). These data supported that the directing binding of triptolide to upstream signaling protein SLC7A11 mediates the downregulation of SLC7A11/GPX4 axis by triptolide.

3.6. Fer-1 Attenuates TIC by Restoring SLC7A11/GPX4 Axis.

Since ferroptosis was demonstrated to be involved in the pathogenesis of TIC, we next explored whether the ferroptosis inhibitor Fer-1 could serve as a potential therapeutic method. As shown in Figures 6(a) and 6(b), Fer-1 significantly rescued triptolide-induced cell death and attenuated corresponding lipid peroxidation. Additionally, intracellular GSH deprivation was ameliorated in the presence of Fer-1 (Figure 6(c)). To gain insights into how Fer-1 scavenged lipid hydroperoxyl radicals, we subsequently investigated the effect of Fer-1 on SLC7A11/GPX4 axis. As shown in Figures 6(d)–6(f), the inhibitory effects of triptolide on SLC7A11/GPX4 axis was partially reversed by Fer-1. Thus, our results suggest Fer-1 as a potential remedy to TIC alleviated ferroptosis through upregulation of the SLC7A11/GPX4 axis to eliminate excess lipid peroxides.

4. Discussion

Triptolide, as the major active component isolated from *Tripterygium wilfordii* Hook F, has attracted enormous interests from pharmaceutical industries and researchers due to its unique activities on rheumatoid arthritis, leukemia, solid tumors, HIV, and autoimmune diseases [2–4]. However, its clinical application is strongly restricted by severe side effects,
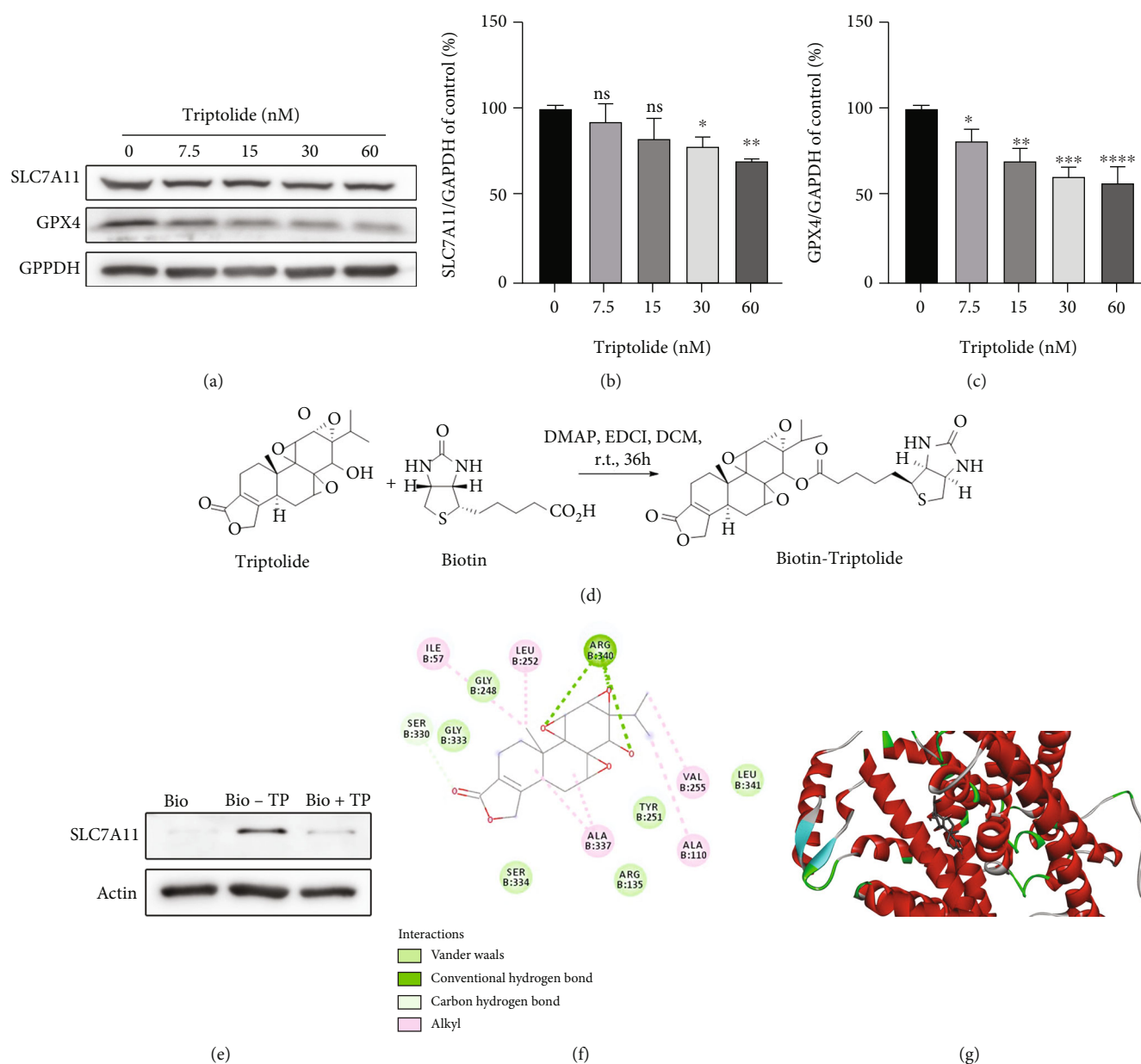
(a)

(b)

(c)

(d)

(e)

(f)

(g)

FIGURE 5: Triptolide downregulates SLC7A11/GPX4 axis by direct binding to SLC7A11. (a) The protein levels of SLC7A11 and GPX4 were measured by Western blots. (b, c) The quantitative analysis of the indicated proteins. (d) The synthesis procedure of biotin-triptolide. (e) Immunoblot with anti-SLC7A11 antibody of protein precipitated by streptavidin beads from AC16 cell lysates in the presence of biotin-triptolide ($10\,\mu M$), biotin ($10\,\mu M$) or the combination of triptolide ($100\,\mu M$), and biotin-triptolide ($10\,\mu M$). (f) Predicted binding sites of triptolide with SLC7A11. (g) Representations of the predicted binding mode of triptolide with SLC7A11. ns: no significant; $^{*}p < 0.05$, $^{**}p < 0.01$, $^{***}p < 0.001$, $^{****}p < 0.0001$ vs. the control group.

especially cardiotoxicity. Emerging evidences have validated that triptolide induces severe cardiotoxicities both *in vivo* and *in vitro*, whereas the underlying mechanism has not been fully elucidated. The major findings from the present study unveiled that ferroptosis, an innovative cell death mode, contributed to TIC. Furthermore, our data suggested that triptolide enhanced intracellular ferrous iron accumulation by reducing iron storage and increasing iron absorption. Excess iron induced ROS accumulation which is further aggravated by the inhibition of Nrf2/HO-1 antioxidant pathway in triptolide-treated AC16 cells. ROS resulted in the overproduc-

tion of lethal lipid peroxides. Meanwhile, the direct inhibitory effects of triptolide on SLC7A11 led to GSH depletion and cascade downregulation of GPX4 which collectively disrupted the clearance of lipid peroxidation and exacerbated ferroptosis. Finally, we found that the ferroptosis inhibitor Fer-1 conferred cardioprotection against TIC through reversing the expression of SLC7A11/GPX4 axis. These findings clarified the molecular events underlying TIC and indicated Fer-1 as a potential therapeutic method for TIC.

Ferroptosis is a nonapoptotic, newly recognized cell death pattern caused by iron-dependent accumulation of
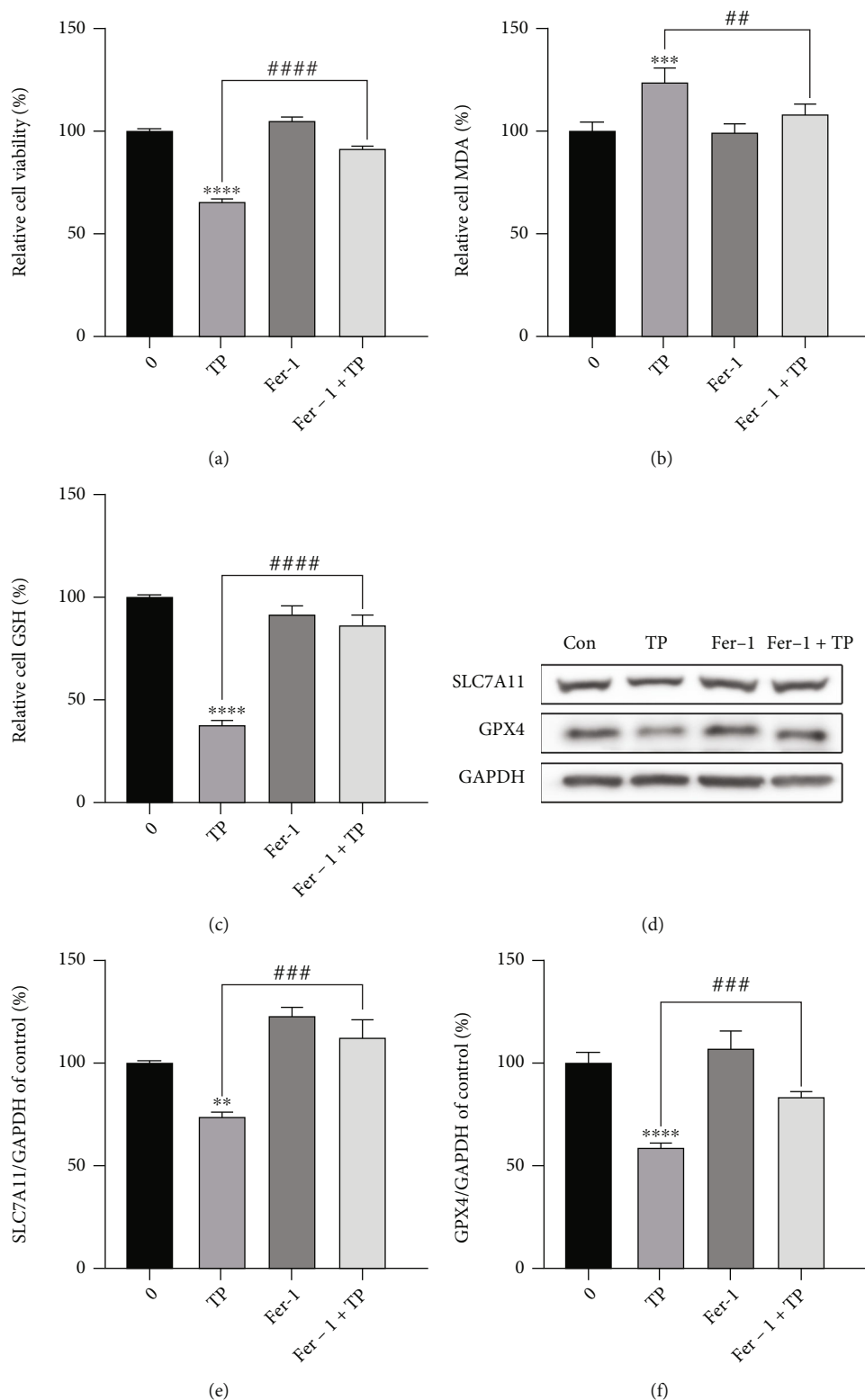
(a)

(b)

(c)

(d)

(e)

(f)

Figure 6: Fer-1 attenuates TIC by restoring SLC7A11/GPX4 axis. (a–d) AC16 cells were pretreated with or without fer-1 ($2 \mu M$) for 1 h and then exposed to triptolide (30 nM) for another 24 h. (a) Cell viability of AC16 cells were detected using CCK8 assays. (b) MDA levels were detected by commercial assay kits. (c) Reduced GSH levels in AC16 cells. (d) The protein levels of SLC7A11 and GPX4 were measured by Western blots. (e, f) The quantitative analysis of the indicated proteins. ****$p < 0.0001$ vs. the control group, ##$p < 0.01$, ###$p < 0.001$, ####$p < 0.0001$ vs. the triptolide group.
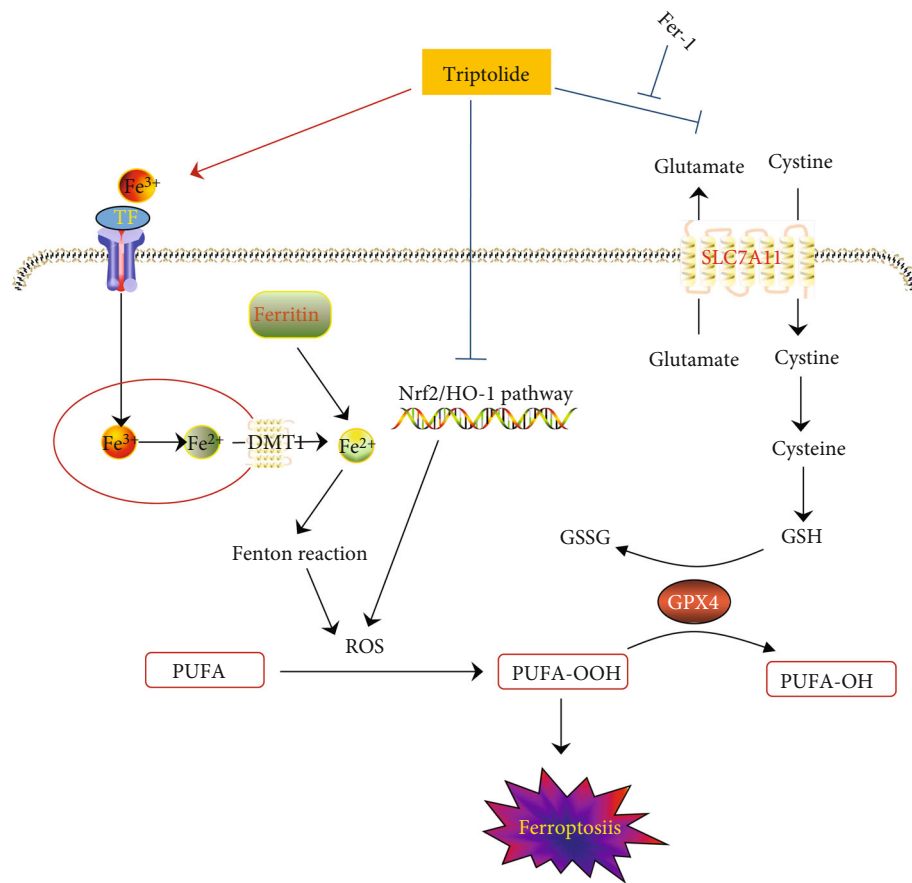
FIGURE 7: Schematic representation of the potential toxic mechanism involved in triptolide-induced ferroptosis.

lipid peroxidation. Recent studies have demonstrated the vital role of ferroptosis in various cardiovascular diseases and drug-induced cardiotoxicities, such as ischemia/reperfusion (I/R)- and doxorubicin-induced cardiac injuries [40]. In this study, RNA-seq and KEGG analysis indicated that ferroptosis may participate in TIC, as related genes involving lipid and iron metabolism enriched significantly. Consistently, we found that triptolide caused lipid peroxidation as indicated by the increase of MDA and 4-HNE levels, iron overload as indicated by rising ferrous iron levels, and GSH depletion as indicated by descending reduced GSH levels. As the key events of ferroptosis, these data further validated that ferroptosis is involved in TIC. Ferroptosis is triggered once the balance between the generation and the clearance of lipid peroxidation is disrupted [41]. Iron overload contributes to the initiation and amplification of lipid peroxides through producing ROS by Fenton reaction. The liable iron pool in the cytoplasm is precisely controlled by an iron import and storage system. Extracellular iron was transported inside with the help of TF/TFRC/DMT1 pathway. The excess iron is stored in the form of ferritin under normal conditions. After triptolide treatment (0-30 nM) for 24 h, the expression of TF, TRFC, and DMT1 increased significantly in a dose-dependent manner, while the expression of FTH1 showed an opposite trend. Upregulation of LC3-II/I ratio indicated the autophagic degradation of FTH1. Interestingly, although the expression of FTH1 continued to

decrease at a higher concentration of triptolide (60 nM), an unexpectedly reduced expressions of TF, TRFC, and DMT1 were observed compared with triptolide stimulation at a concentration of 30 nM. We thought this phenomenon may act as the compensatory mechanism to antagonize the progressively higher level of intracellular iron.

Nrf2/HO-1 pathway, a classic antioxidant pathway, has been proved as a defensive response against ferroptosis in many studies. Emerging as a potential target, activation of Nrf2/HO-1 pathway has shown to be an effective way to attenuate ferroptosis-induced injuries and diseases, including LPS-induced acute lung injury [42], contusion spinal cord injury [43], type 2 diabetic osteoporosis [44], and radiation-induced intestinal epithelial cell death [45]. In our hand, we found that triptolide showed potent inhibition on Nrf2/HO-1 pathway, which disrupted the elimination of ROS. ROS accumulation driven by iron overload and further exacerbated by inactivation of Nrf2/HO-1 antioxidant pathway synergistically resulted in the excess generation of lethal lipid peroxides. These results were in line with the previous findings [42–47].

Reduced GSH is an essential intracellular antioxidant synthesized from glutamate, cysteine, and glycine, which works together with GPX4 to converts toxic lipids to nontoxic lipids [48]. The rate of glutathione synthesis is limited by cysteine availability. SLC7A11 mediates the import of extracellular cystine that is to be converted to cysteine by

GSH or TXNRD1. The inhibition of SLC7A11 will lead to GSH exhaustion thus directly impacting on GPX4 activity and stability and thereby predisposing cells to ferroptosis. In the streptavidin-biotin affinity pull-down assay, triptolide exhibited direct and strong affinity with SLC7A11. Computational molecular docking indicated that triptolide could interact with amino acid residues on SLC7A11 by van der Waals, carbon hydrogen bond, conventional hydrogen bond, and alkyl. In addition, triptolide inhibited the expression of SLC7A11 and GPX4. Taken together, triptolide led to exhaustion of GSH and deteriorated the clearance of lethal lipid peroxides through direct inhibition on SLC7A11 and cascade downregulation of GPX4. Fer-1, as the ferroptosis inhibitor, has been extensively investigated in various ferroptosis-related diseases. Cumulative evidences suggested Fer-1 attenuated ferroptosis by targeting at SLC7A11/GPX4 pathway. In this study, the application of Fer-1 potently rescued triptolide-induced cytotoxicity and reversed ferroptosis-related events including the accumulations of MDA iron. In-depth studies unveiled that the downregulation of SLC7A11 and GPX4 could be alleviated by Fer-1. These data indicated Fer-1 as a potential therapeutic approach to TIC.

5. Conclusion

Our current study found that TIC was causatively associated with ferroptosis. As shown in Figure 7, triptolide induced iron overload by dysregulation of iron metabolism which led to ROS accumulation through Fenton reaction. Meanwhile, triptolide impeded ROS elimination *via* inactivation of Nrf2/HO-1 antioxidant system. Excess ROS triggered the overproduction of lethal lipid peroxides. In addition, triptolide-induced GSH depletion hindered the clearance of lipid peroxides and promoted ferroptosis by direct inhibition on SLC7A11 and cascade downregulation on GPX4. Fortunately, Fer-1 could alleviate triptolide-induced ferroptosis through restoring SLC7A11/GPX4 pathway. In summary, our study provided a new insight into the underlying mechanisms of TIC and presented a potential therapeutic strategy for circumventing this side effects.

Triptolide induced intracellular iron overload through dysregulating TF/TFRC/DMT1/FTH1 pathway which mediated iron absorption and storage. Excess iron contributed to ROS generation via Fenton reaction. The inhibitory effects of triptolide on antioxidant Nrf2/HO-1 pathway exacerbated ROS accumulation which led to overproduction of lethal lipid peroxides. Furthermore, triptolide directly bound to SLC7A11 to inactivate SLC7A11/GPX4 axis which functioned to detoxify of toxic lipid peroxides to nontoxic lipid alcohols. Fer-1 alleviated triptolide-induced ferroptosis via partially reversing the inhibitory effects of triptolide on SLC7A11/GPX4 signal.

Data Availability

The data used to support the findings of this study are included within the article and supporting information.

Conflicts of Interest

The authors have no conflicts of interest to declare.

Authors' Contributions

Xian Liu, Cheng Chen, and Dong Han contributed equally to this work.

Supplementary Materials

A detailed description of the synthesis method of triptolide-biotin and its related spectra were provided in the Supporting Information. *(Supplementary Materials)*

References

[1] P. Noel, D. Von Hoff, A. Saluja, M. Velagapudi, E. Borazanci, and H. Han, "Triptolide and its derivatives as cancer therapies," *Trends in Pharmacological Sciences*, vol. 40, no. 5, pp. 327–341, 2019.

[2] K. Yuan, X. Li, Q. Lu et al., "Application and mechanisms of triptolide in the treatment of inflammatory diseases-a review," *Frontiers in Pharmacology*, vol. 10, article 1469, 2019.

[3] I. R. Dias, H. H. Lo, K. Zhang et al., "Potential therapeutic compounds from traditional Chinese medicine targeting endoplasmic reticulum stress to alleviate rheumatoid arthritis," *Pharmacological Research*, vol. 170, article 105696, 2021.

[4] J. Cai, M. Yi, Y. Tan et al., "Natural product triptolide induces GSDME-mediated pyroptosis in head and neck cancer through suppressing mitochondrial hexokinase-*II*," *Journal of Experimental & Clinical Cancer Research*, vol. 40, no. 1, p. 190, 2021.

[5] L. Tong, Q. Zhao, E. Datan et al., "Triptolide: reflections on two decades of research and prospects for the future," *Natural Product Reports*, vol. 38, no. 4, pp. 843–860, 2021.

[6] C. Xi, S. Peng, Z. Wu, Q. Zhou, and J. Zhou, "Toxicity of triptolide and the molecular mechanisms involved," *Biomedicine & Pharmacotherapy*, vol. 90, pp. 531–541, 2017.

[7] J. Zhou, C. Xi, W. Wang et al., "Triptolide-induced oxidative stress involved with Nrf2 contribute to cardiomyocyte apoptosis through mitochondrial dependent pathways," *Toxicology Letters*, vol. 230, no. 3, pp. 454–466, 2014.

[8] W. Wang, Y. Yang, J. Xiong et al., "Inhibition of glycogen synthase kinase 3beta ameliorates triptolide-induced acute cardiac injury by desensitizing mitochondrial permeability transition," *Toxicology and Applied Pharmacology*, vol. 313, pp. 195–203, 2016.

[9] Y. Yang, W. Wang, Z. Xiong et al., "Resveratrol protects against triptolide-induced cardiotoxicity through SIRT3 signaling pathway <i>in vivo</i> and <i>in vitro</i>," *Die Pharmazie*, vol. 71, no. 9, pp. 514–523, 2016.

[10] S. Wang, X. Chen, S. Ling, R. Ni, H. Guo, and J. Xu, "MicroRNA expression, targeting, release dynamics and early-warning biomarkers in acute cardiotoxicity induced by triptolide in rats," *Biomedicine & Pharmacotherapy*, vol. 111, pp. 1467–1477, 2019.

[11] Y. Xi, W. Wang, L. Wang et al., "Triptolide induces p53-dependent cardiotoxicity through mitochondrial membrane permeabilization in cardiomyocytes," *Toxicology and Applied Pharmacology*, vol. 355, pp. 269–285, 2018.

[12] Y. Yang, W. Wang, Z. Xiong et al., "Activation of SIRT3 attenuates triptolide-induced toxicity through closing mitochondrial permeability transition pore in cardiomyocytes," *Toxicology In Vitro*, vol. 34, pp. 128–137, 2016.

[13] J. Zhou, C. Xi, W. Wang, Y. Yang, Y. Qiu, and Z. Huang, "Autophagy plays an important role in triptolide-induced apoptosis in cardiomyocytes," *Toxicology Letters*, vol. 236, no. 3, pp. 168–183, 2015.

[14] W. Yang and B. Stockwell, "Ferroptosis: death by lipid peroxidation," *Trends in Cell Biology*, vol. 26, no. 3, pp. 165–176, 2016.

[15] J. Li, F. Cao, H. Yin et al., "Ferroptosis: past, present and future," *Cell Death & Disease*, vol. 11, no. 2, p. 88, 2020.

[16] X. Fang, H. Wang, D. Han et al., "Ferroptosis as a target for protection against cardiomyopathy," *PNAS*, vol. 116, no. 7, pp. 2672–2680, 2019.

[17] W. Ma, S. Wei, B. Zhang, and W. Li, "Molecular mechanisms of cardiomyocyte death in drug-induced cardiotoxicity," *Frontiers in Cell and Development Biology*, vol. 8, p. 434, 2020.

[18] Y. Liu, L. Zeng, Y. Yang, C. Chen, D. Wang, and H. Wang, "Acyl-CoA thioesterase 1 prevents cardiomyocytes from doxorubicin-induced ferroptosis via shaping the lipid composition," *Cell Death & Disease*, vol. 11, no. 9, p. 756, 2020.

[19] T. Tadokoro, M. Ikeda, T. Ide et al., "Mitochondria-dependent ferroptosis plays a pivotal role in doxorubicin cardiotoxicity," *JCI Insight*, vol. 5, no. 9, article e132747, 2020.

[20] B. Stockwell, J. Friedmann Angeli, H. Bayir et al., "Ferroptosis: a regulated cell death nexus linking metabolism, redox biology, and disease," *Cell*, vol. 171, no. 2, pp. 273–285, 2017.

[21] A. Bogdan, M. Miyazawa, K. Hashimoto, and Y. Tsuji, "Regulators of iron homeostasis: new players in metabolism, cell death, and disease," *Trends in Biochemical Sciences*, vol. 41, no. 3, pp. 274–286, 2016.

[22] M. Morales and X. Xue, "Targeting iron metabolism in cancer therapy," *Theranostics*, vol. 11, no. 17, pp. 8412–8429, 2021.

[23] B. Hassannia, P. Vandenabeele, and T. Bergh, "Targeting ferroptosis to iron out cancer," *Cancer Cell*, vol. 35, no. 6, pp. 830–849, 2019.

[24] J. Zheng and M. Conrad, "The metabolic underpinnings of ferroptosis," *Cell Metabolism*, vol. 32, no. 6, pp. 920–937, 2020.

[25] P. Koppula, L. Zhuang, and B. Gan, "Cystine transporter SLC7A11/xCT in cancer: ferroptosis, nutrient dependency, and cancer therapy," *Protein & Cell*, vol. 12, no. 8, pp. 599–620, 2021.

[26] H. Yan, T. Zou, Q. Tuo et al., "Ferroptosis: mechanisms and links with diseases," *Signal Transduction and Targeted Therapy*, vol. 6, no. 1, p. 49, 2021.

[27] Y. Xie, W. Hou, X. Song et al., "Ferroptosis: process and function," *Cell Death and Differentiation*, vol. 23, no. 3, pp. 369–379, 2016.

[28] X. Wu, Y. Li, S. Zhang, and X. Zhou, "Ferroptosis as a novel therapeutic target for cardiovascular disease," *Theranostics*, vol. 11, no. 7, pp. 3052–3059, 2021.

[29] G. Zou, X. Zhang, L. Wang et al., "Herb-sourced emodin inhibits angiogenesis of breast cancer by targeting VEGFA transcription," *Theranostics*, vol. 10, no. 15, pp. 6839–6853, 2020.

[30] S. Du, X. Song, Y. Li et al., "Celastrol inhibits ezrin-mediated migration of hepatocellular carcinoma cells," *Scientific Reports*, vol. 10, no. 1, p. 11273, 2020.

[31] H. Berman, J. Westbrook, Z. Feng et al., "The Protein Data Bank," *Nucleic Acids Research*, vol. 28, no. 1, pp. 235–242, 2000.

[32] K. Oda, Y. Lee, P. Wiriyasermkul et al., "Consensus mutagenesis approach improves the thermal stability of system x c - transporter, xCT, and enables cryo-EM analyses," *Protein Science*, vol. 29, no. 12, pp. 2398–2407, 2020.

[33] N. Zhou and J. Bao, "FerrDb: a manually curated resource for regulators and markers of ferroptosis and ferroptosis-disease associations," *Database: The Journal of Biological Databases and Curation*, vol. 2020, article baaa021, 2020.

[34] S. J. Dixon, K. M. Lemberg, M. R. Lamprecht et al., "Ferroptosis: an iron-dependent form of nonapoptotic cell death," *Cell*, vol. 149, no. 5, pp. 1060–1072, 2012.

[35] S. Masaldan, S. Clatworthy, C. Gamell et al., "Iron accumulation in senescent cells is coupled with impaired ferritinophagy and inhibition of ferroptosis," *Redox Biology*, vol. 14, pp. 100–115, 2018.

[36] L. Su, J. Zhang, H. Gomez et al., "Reactive oxygen species-induced lipid peroxidation in apoptosis, autophagy, and ferroptosis," *Oxidative Medicine and Cellular Longevity*, vol. 2019, Article ID 5080843, 13 pages, 2019.

[37] M. Dodsona, R. Castro-Portugueza, and D. Zhang, "NRF2 plays a critical role in mitigating lipid peroxidation and ferroptosis," *Redox Biology*, vol. 23, article 101107, 2019.

[38] L. Pinzi and G. Rastelli, "Molecular docking: shifting paradigms in drug discovery," *International Journal of Molecular Sciences*, vol. 20, no. 18, article 4331, 2019.

[39] G. Sliwoski, S. Kothiwale, J. Meiler, and E. Lowe, "Computational methods in drug discovery," *Pharmacological Reviews*, vol. 66, no. 1, pp. 334–395, 2014.

[40] M. Li, Z. Wang, L. Fang, S. Cheng, X. Wang, and N. Liu, "Programmed cell death in atherosclerosis and vascular calcification," *Cell Death & Disease*, vol. 13, no. 5, p. 467, 2022.

[41] M. Wang, C. Liu, T. Wang et al., "(+)-Clausenamide protects against drug-induced liver injury by inhibiting hepatocyte ferroptosis," *Cell Death & Disease*, vol. 11, no. 9, p. 781, 2020.

[42] J. Li, K. Lu, F. Sun et al., "Panaxydol attenuates ferroptosis against LPS-induced acute lung injury in mice by Keap 1-Nrf2/HO-1 pathway," *Journal of Translational Medicine*, vol. 19, no. 1, p. 96, 2021.

[43] M. Ge, H. Tian, L. Mao et al., "Zinc attenuates ferroptosis and promotes functional recovery in contusion spinal cord injury by activating Nrf2/GPX4 defense pathway," *CNS Neuroscience & Therapeutics*, vol. 27, no. 9, pp. 1023–1040, 2021.

[44] H. Ma, X. Wang, W. Zhang et al., "Melatonin suppresses ferroptosis induced by high glucose via activation of the Nrf2/HO-1 signaling pathway in type 2 diabetic osteoporosis,"

Oxidative Medicine and Cellular Longevity, vol. 2020, Article ID 9067610, 18 pages, 2020.

[45] L. Xie, S. Cai, T. Zhao, M. Li, and Y. Tian, "Green tea derivative (−)-epigallocatechin-3-gallate (EGCG) confers protection against ionizing radiation-induced intestinal epithelial cell death both *in vitro* and *in vivo*," *Free Radical Biology & Medicine*, vol. 161, pp. 175–186, 2020.

[46] J. Roh, E. Kim, H. Jang, and D. Shin, "Nrf2 inhibition reverses the resistance of cisplatin-resistant head and neck cancer cells to artesunate-induced ferroptosis," *Redox Biology*, vol. 11, pp. 254–262, 2017.

[47] H. Deng, L. Yue, N. Wang et al., "Mitochondrial iron overload-mediated inhibition of Nrf2-HO-1/GPX4 assisted ALI-induced nephrotoxicity," *Frontiers in Pharmacology*, vol. 11, article 624529, 2021.

[48] W. S. Yang, R. SriRamaratnam, M. E. Welsch et al., "Regulation of ferroptotic cancer cell death by GPX4," *Cell*, vol. 156, no. 1-2, pp. 317–331, 2014.